Airborne Broadband Ultrasound: Wireless Channel and Motion Tracking Algorithms

Mohammed Alloulah

Airborne Broadband Ultrasound: Wireless Channel and Motion Tracking Algorithms

Mohammed Alloulah* et al.

***Abstract*—Airborne broadband ultrasound (ABU) covers a wide stretch of inaudible acoustic frequencies which have been used to provide scalable (i.e. multiuser) and highly robust ranging and localization of static tags in indoor environments. This is useful for mobile computing applications and robotics. However, because ABU signals are wideband and propagate relatively slowly, they are prone to aggressive Doppler distortion as a result of human-scale movements indoors. Additionally, the ABU channel is characterized by pronounced distance-dependent variations. This paper gives a treatment of the ABU channel both theoretically and experimentally, in order to inform the design of ABU tracking systems. Then, Doppler-tolerant ABU tracking algorithms are developed. Their performance is reported, using a direct-sequence (DS) code-division multiple access (CDMA) signalling approach. Successful motion inference is demonstrated in the ABU band.**

I. Introduction

HIGH-resolution tracking of people and mobile devices in buildings is of great significance to a number of application domains for example: a handheld moving map for indoor navigation, "throwing" video content from a mobile phone to a wall-mounted display using gesture-based interaction, and emergency search and rescue and live coordination of personnel at disaster sites. In this paper, the term *tracking* is used to encompass both the initial position estimation of a person or object, followed by the continual monitoring of movement thereafter.

Accurate, *fine-grained* indoor tracking has been classically achieved by infrastructure-reliant systems, using ultra-wideband (UWB) radio, optical or magnetic sensing [1]. Ultrasonic sensing has also been used for the provision of tracking services indoors [2]. Compared to radio, the low frequency and propagation rate of airborne ultrasound yields advantages in accuracy, processing requirements, and ease of installation. However most systems to date have used piezoceramic transducers which have a usable bandwidth of less than five kilohertz. Such narrowband ultrasound poses restrictions on the real-world utility of these tracking systems, especially in scenarios where multiple users must be tracked concurrently, or environments with aggressive ultrasonic noise.

The use of broadband ultrasound in-air was first shown to afford a number of system-level enhancements to tracking [3]; this was demonstrated using a curved piezo film transducer design [4] with a measured bandwidth of 40 kHz and code division multiple access (CDMA) signalling [3]. Others have since explored performance using MEMS transducer technology (bandwidth 15 kHz), and frequency-hopped signalling [5]. Another related work investigated the outdoor performance (bandwidth 14 kHz) also using direct-sequence (DS) signalling [6]. Close in spirit too, a communications work assessed airborne ultrasound's short-range ability to carry data using a practical bandwidth between 120 to 200 kHz with a bit rate of 200 kb/s [7]. However, the literature lacks a formal model for the airborne broadband ultrasonic channel, which is needed to better inform the design of future ABU tracking systems. Moreover, coded broadband ultrasonic signals are prone to significant Doppler distortion even in the presence of relatively slow rates of indoor movement, such as walking (1 m/s or faster). Consequently, elaborate tracking applications are best supported if ABU signals can continue to be detected in the presence of Doppler shifting.

This paper has two primary contributions. First, it provides (section II) a new description of the ABU channel. An information theoretic analysis to ABU is given in order to highlight the peculiarities of the channel, followed by statistical characterization using real ABU signals. Second, phase coherent direct sequence (DS) CDMA tracking for moving ABU tags is derived (section III), leading to two algorithmic configurations that belong to different classes of instantaneous frequency estimators. Empirical performance (section IV) of the two tracker configurations is then reported.

II. Channel Model

In this section, the development of a channel model for ABU follows closely that of its underwater acoustics kin [8].

A. Acoustic Propagation

The overall attenuation that characterizes the propagation of airborne acoustics indoors is given by

$$A(l,f) = l^{\beta} \cdot \alpha(f)^{l} \tag{1}$$

$$A(l,f)\Big|_{dB} = \beta \cdot 10\log l + l \cdot 10\log \alpha(f) \tag{2}$$

where l denotes the distance from the source and f is the signal frequency. As evident from equation (2), the propagation of sound in free air is governed by two main phenomena: spreading and absorption. The parameter β models the spreading loss pattern, and assumes values between 1 and 2. The second term models the distance and frequency-dependent absorption of airborne acoustics, with the coefficient $\alpha(f)$.

Formulae for calculating the absorption rate per meter at a single discrete frequency are previously developed [9], [10].

*E-mail: alloulah@outlook.com

Backdated: 11 July 2012; Version 1.0.

Manuscript had originally two other co-authors in addition to the primary author currently withheld pending their approval.

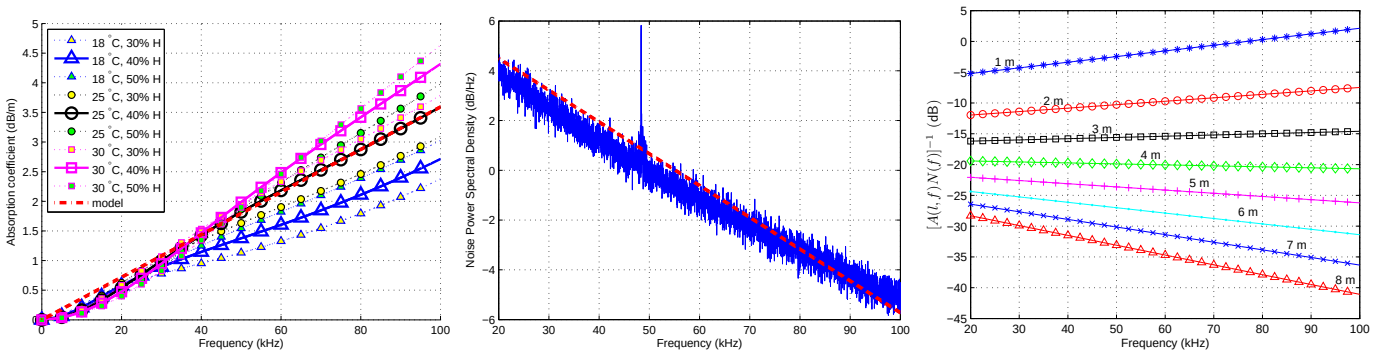

(a) Acoustic absorption in air (dB/m). (b) PSD of the receiver noise floor. (c) The $A(l,f)N(f)$ product.

Fig. 1: The dependency of SNR in the ABU channel on frequency and distance.

Using these formulae, figure 1a illustrates the distance and frequency-dependent absorption coefficient of the airborne acoustics of interest. Always calculated at one standard atmospheric pressure, nine reference temperature and humidity permutations are shown in order to give a flavour for the behaviour of the absorption coefficient indoors.

Typically, with a temperature of 25° Celsius and a humidity of 40%, the absorption coefficient can be conveniently approximated at by

$$10\log\alpha(f) = 0.03592 \times 10^{-3} f \tag{3}$$

as indicated by the dashed line in figure 1a.

B. Signal-to-Noise Ratio

1) Noise generated by receiver: The broadband receiver exhibits variability in terms of the ever present thermal noise across its frequency range. In order to account for this effect in the overall channel model, the receiver's ambient noise is next characterized using a dataset collected from a typical office environment.

Six seconds of data are collected at a sampling rate of 500 kHz. The power spectral density (PSD) of the receiver's ambient noise is estimated using the Welch averaged modified periodogram method. The PSD is referenced to the AC power density of receiver's bandwidth center (50 kHz), which is also the average AC power density of the recorded six-second sequence.

Figure 1b shows that a gradual decay of around 10 dB across the ultrasonic band characterizes in general the ambient noise PSD at the receiver. Outstanding ultrasonic noise spikes can be radiated by everyday indoor machinery, such as air conditioning fans. This is evident in figure 1b with the group of narrowband harmonics just below 50 kHz. While such ambient ultrasonic noise will vary subject to the specifics of a given indoor environment, the general noise behaviour of the broadband receiver can be approximately modelled as

$$N(f)\Big|_{dB} = 10\log N(f) = 7.0560 - 0.1278 \times 10^{-3} f \tag{4}$$

where f is the frequency in Hz and the noise in decibels is referenced to 50 kHz as pointed to above. The noise model is illustrated by the dashed line in figure 1b.

2) SNR: The expressions for the attenuation $A(l,f)$ and noise $N(f)$ can be combined to arrive at a frequency and distance-dependent signal-to-noise ratio (SNR) for the ABU channel, similar to underwater acoustics (UWA) [8]. In this ABU formulation, the SNR does not factor in explicitly ambient noise—the accurate ambient noise PSD is dependent on a particular indoor environment. Nonetheless, it still provides a very informative account on the frequency and range variability of the SNR in the ABU channel. This variability translates into range-dependent bandwidth given a constant transmission power. Sophisticated power control in ABU should take advantage of this model in order to optimize bandwidth and capacity in a mobile medium with non-equidistant co-located users. Specifically, the most comprehensive power control could employ pre/de-emphasis techniques using this frequency and distance-dependent SNR model along with estimates of the range and speed of mobile users.

Defining a narrow band of frequencies Δf around a single frequency f, the SNR is expressed as

$$SNR(l,f) = \frac{\mathcal{P}}{A(l,f)N(f)\Delta f} \tag{5}$$

where $\mathcal{P}$ is the power of the signle frequency f.

From expression (5), we note that the variability in SNR is characterized by the factor $1/A(l,f)N(f)$. Thus, this frequency and distance-dependent factor can be used in order to characterize SNR in the ABU channel. Figure 1c depicts such a factor evaluated at eight distances across the frequency span of interest, with a spherical spreading parameter of $\beta = 2$.

Near and far distances give rise to the most variability across the the wide frequency band of interest ([30 kHz, 70 kHz] in our system). At 1 meter, around 3.67 dB variability is in favour of higher frequencies, whereas at 8 meters, about 6.39 dB is in favour of lower frequencies. At 3 and 4 meters, SNR varies little across the frequency band to around 0.8 and 0.64 dB, respectively.

The $A(l,f)N(f)$ product is linear in dB with a slope that is dependent on distance. This fact gives rise to an optimal frequency $f_o(l)$ at which the narrowband SNR is maximized. Such optimal frequency is plotted versus distance in figure 2. Next we will elaborate on one optimization criterion by means

of which the capacity of a mobile ABU channel with non-equidistant co-located users could be improved.

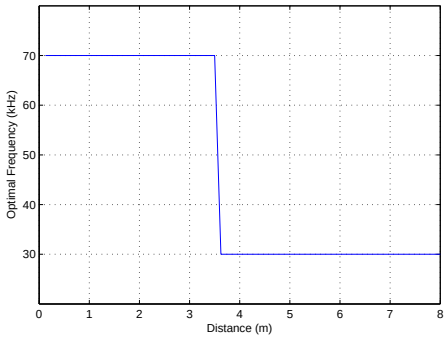

Fig. 2: The optimal frequency that maximizes SNR.

C. Bandwidth and Capacity

In a mobile ABU tracking system, the capacity of the channel influences greatly the system's quality of service. That is, both the tracking update rate and number of participating users are increased with the enhancing of the channel's capacity.

Assuming a linear time-invariant channel during some observation interval, the overall capacity can be seen as the summation of a number of sub-narrowband capacities. That is, if the bandwidth is divided into I narrow sub-bands each of width Δf and a noise PSD $N(f_i)$—noise can be approximated as Gaussian—then the overall capacity is given as

$$C(l) = \sum_{i=1}^{I} \Delta f \log_2 \left[1 + \frac{S_l(f_i) A^{-1}(l, f_i)}{N(f_i)} \right] \tag{6}$$

where $S_l(f_i)$ is the i^{th} frequency bin PSD of the transmitted signal designed to propagate over distance l. The optimal PSD $S_l(f)$ which will maximize the capacity is given by [11, p. 745]

$$S_l(f) + A(l, f)N(f) = K_l \tag{7}$$

where K_l is a constant related to the total power constraint $P(l)$, and $S_l(f) \geq 0$.

In turn, the power $P(l)$ is related to SNR as

$$P(l) = \int_{B(l)} S_l(f) df \tag{8}$$

$$SNR\big(l, B(l)\big) = \frac{\int_{B(l)} S_l(f) A^{-1}(l, f) df}{\int_{B(l)} N(f) df} \tag{9}$$

Varying K_l according to the optimization criterion of equation (7) provides a means for achieving an SNR objective SNR_0 and a pre-specified transmission power. This can be seen by substituting equation (7) into equations (8) & (9) so as to obtain

$$P(l) = K_l B(l) - \int_{B(l)} A(l, f)N(f) df \tag{10}$$

$$SNR\big(l, B(l)\big) = K_l \frac{\int_{B(l)} A^{-1}(l, f) df}{\int_{B(l)} N(f) df} - 1 \tag{11}$$

The details of a numerical procedure for arriving at $S_l(f)$ that maximizes capacity are supplied by Stojanovic [8]. After such optimization, the distance-dependent transmission PSD is given by

$$S_l(f) = \begin{cases} K_l - A(l, f)N(f), & f \in B(l) \\ 0, & \text{otherwise} \end{cases} \tag{12}$$

with the overall channel capacity being calculated from

$$C(l) = \int_{B(l)} \log_2 \left[\frac{K_l}{A(l, f)N(f)} \right] df \tag{13}$$

D. Numerical Model

The capacity-based model given previously is evaluated numerically next. As stated before, the bandwidth of interest is between 30 kHz and 70 kHz—outside this range, analysis is meaningless due to physical transduction limitations. A typical indoor temperature of 25° Celsius and a humidity of 40% are chosen. A spherical spreading factor of $\beta = 2$ is used. The SNR objective SNR_0 is swept from -13 dB to 20 dB in 3 dB increments.

The effect of SNR on bandwidth allocation per distance is examined in figure 3a. The different slopes of the $A(l, f)N(f)$ product (figure 1c) result in a large bandwidth allocation variance across distances when operating in a low SNR regime. This is then gradually enhanced with the increasing of SNR until bandwidth becomes almost uniform starting at $SNR_0 = -2$ dB (not shown), which is in line with Shannon's limit on reliable communication at -1.6 dB [11, p. 207].

The capacity follows a similar pattern to that of the bandwidth as shown in figure 3b. The capacity peaks at the middle of the distance range in the low SNR regime owing to the almost constant $A(l, f)N(f)$ product. At $SNR_0 = 4$ dB, the capacity takes on a consistent shape whereby the channel changes little at farther distances. It is also observed that beyond $SNR_0 = 1$ dB, enhancements brought about with the increasing of SNR tend to diminish in comparison with those in the low SNR regime.

The power in micro Pascals is depicted in figure 3c. Affected by the bandwidth and capacity observations, around 40 dB transmission is required to clear the low SNR regime. Under the optimal capacity definition of bandwidth, this may or may not be possible to accommodate depending on a number of contending factors such as sound exposure safety, transducer excitation limitations, and operational volume. The 3 dB increments in SNR objective steadily offset the power curve in the high SNR regime.

A utilization measure of the available bandwidth is the bandwidth over capacity B/C ratio. To investigate the effect of SNR on the the utilization of the ABU channel, the B/C

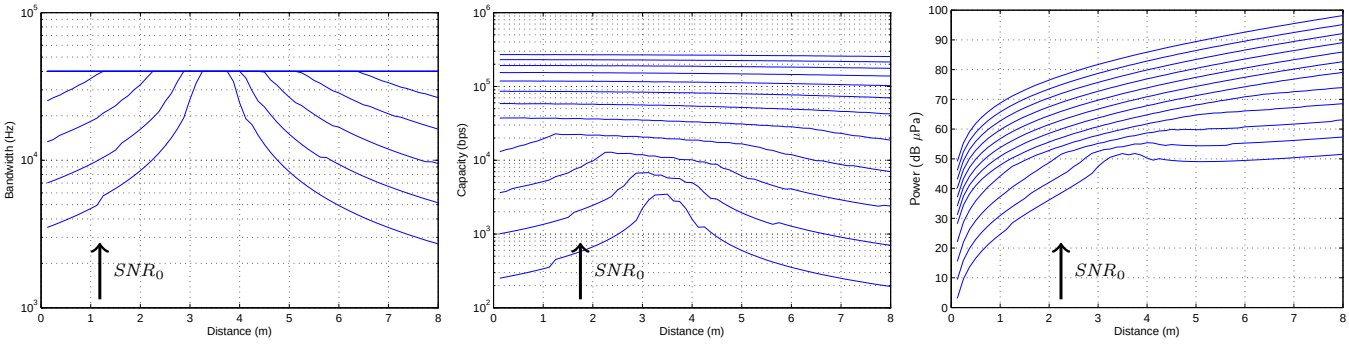

(a) bandwidth allocation (b) channel capacity (c) power

Fig. 3: The effect of SNR on $(\cdot)$ versus distance.

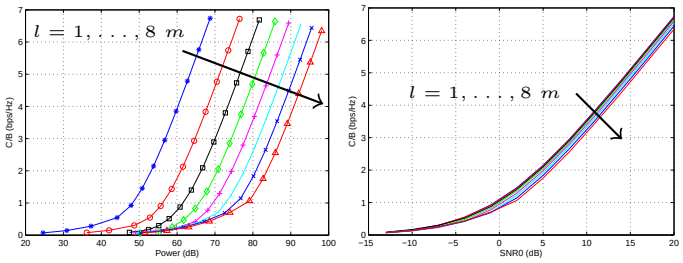

(a) power (b) SNR

Fig. 4: B/C ratio versus $(\cdot)$.

ratio at various distances is plotted in figure 4 against power and against SNR in 4a and 4b, respectively. Expectedly, the B/C ratio increases with power and SNR.

E. Time Variability

Away from the mobility-induced Doppler effect, the airborne acoustic channel indoors is influenced by factors such as temperature and humidity. Other contributors also affect the operation of the acoustic medium such as air conditioning drafts and noise emanating from everyday human activities. These factors are hard to model accurately in dynamic living environments and assessing their aggregate effect statistically remains the only viable approach at understanding the seemingly random changes in the airborne acoustic channel.

To this end, a transmitter-receiver pair was placed at an approximate distance of 2.25 m. The receiver was carefully oriented next to a smooth hard surface as to detect two path arrivals, direct and reflected. A Gold code sequence of length 511 was BPSK-modulated onto a 50 kHz carrier at a 20 kHz chip rate. A continuous transmission of about 18 seconds was recorded. The channel impulse response as obtained by correlation is shown in figure 5. The channel consists of a direct path and a reflected path which is always more attenuated as a result of the loss in acoustic energy. The variations over time in the magnitude and phase of the two path arrivals are also illustrated in figure 5, along with the respective histograms. These histograms suggest a Rician or even Gaussian distribution for the magnitude of two arrivals; while the phase seems to follow a uniform distribution. Nonetheless, further investigation is needed before formalizing the statistical

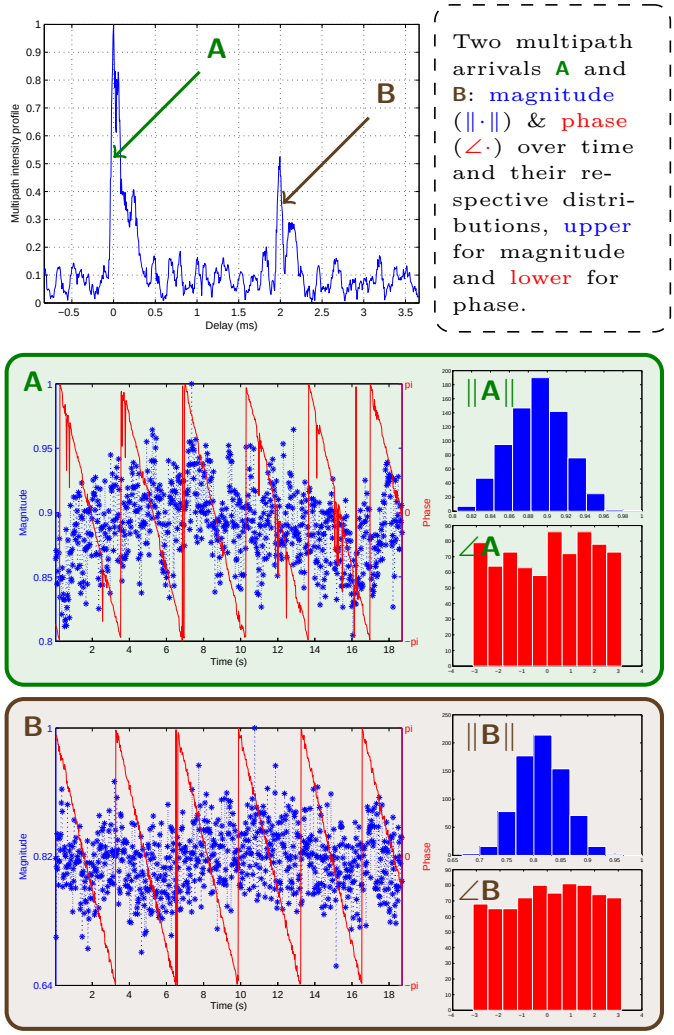

Fig. 5: Multipath intensity profile.

nature of multipath in ABU under dynamic environmental conditions indoors.

III. Tracking

This section focuses on direct-sequence spread spectrum (DSSS) modulation. DSSS allows for explicit self and multiuser-interference models that are computationally

tractable, and as such highly amenable to embedded real-time realizations. Such real-time realizations were investigated by Alloulah using a high-level synthesis (HLS) methodology [12].

A. DSSS System Model

The complex baseband signal at the receiver is modelled as

$$v(t) = \sum_m q(m)h(t - mT_c) \times e^{j\theta(t)} + w(t) \tag{14}$$

where q is the spreading code, $h(t)$ is the channel impulse response which accounts for transmitter and receiver filtering, T_c is the chip duration, $\theta(t)$ is a phase function modeling the aggregate offset and/or distortion resulting from transmitter-receiver oscillator mismatch and/or mobility respectively, and $w(t)$ is an additive noise which is assumed to be uncorrelated with the signal.

At the receiver, the signal is oversampled by N_s samples per chip and arranged in a column vector spanning the spreading code length L and whose topmost entry is the most recent input sample. The received signal vector expressed as the spreading code convolved with the channel can now be rewritten in vector format as

$$\mathbf{v}(k) = \sum_m \mathbf{h}[m]q[k-m] \cdot e^{j\boldsymbol{\theta}(k)} + \mathbf{w}(k) \tag{15}$$

where

$$\mathbf{v}(k) = \begin{bmatrix} \underline{\mathbf{v}}_{L-1}(k) \\ \vdots \\ \underline{\mathbf{v}}_0(k) \end{bmatrix}, \ \mathbf{h}(k) = \begin{bmatrix} \underline{\mathbf{h}}_{L-1}(k) \\ \vdots \\ \underline{\mathbf{h}}_0(k) \end{bmatrix} = \mathbf{h}[0] \tag{16}$$

are $LN_s \times 1$ vectors whose entries $\underline{\mathbf{v}}_l(k)$ and $\underline{\mathbf{h}}_l(k)$ are partial vectors containing the l^{th} chip-worth of samples and the fractional channel coefficient, respectively.

Further, noting the causality of the system, $\mathbf{h}[m]$ in the convolution kernel is defined as $\mathbf{h}(k)$ shifted down by $m \times N_s$ samples.

$$\mathbf{h}[m] = \begin{bmatrix} \underbrace{\underline{\mathbf{0}} \\ \vdots}_{m} \\ \underline{\mathbf{h}}_{L-1}(k) \\ \vdots \\ \underline{\mathbf{h}}_m(k) \end{bmatrix} \tag{17}$$

$$\boldsymbol{\theta}(k) = \begin{bmatrix} \theta(k+L-1) \\ \vdots \\ \theta(k) \end{bmatrix} \tag{18}$$

Similarly, $q[\cdot]$ denotes modulo-L addressing of the spreading sequence. Also, $\boldsymbol{\theta}(k)$ is a vector containing L-chip phase deviations that are multiplied element-wise with their respective L $\underline{\mathbf{v}}_l(k)$ as denoted with the dot operator $\cdot$ in equation (15). Lastly, $\mathbf{w}(k)$ is an $LN_s \times 1$ vector of additive noise.

B. Receiver Algorithm

The proposed receiver structure is one that is user-oriented, decoupled, and extensible. A block abstraction of the receiver is presented in figure 6.

The derivation will proceed in a step-by-step manner to build hybrid Doppler-tolerant trackers. This approach is important owing to the absence of prior experience on phase tracking in the novel ABU band, hence the need to consider different methods in order to assess their utility in ABU and its applications.

1) Core DS CDMA Adaptive Engine: This subsection along with subsection III-B3 follow closely the derivation of Stajanovic et al. [13]. Later subsections will depart—building in places on the intuition from [14] and [15]—to introduce the feedforward filter and linear interpolator stages developed for ABU.

a) Channel-based formulation: The acquisition algorithm is based on the fact that noise is uncorrelated with the spreading sequence

$$\mathbf{h}(k) = \mathbf{E}\Big\{\mathbf{v}(k) \cdot e^{-j\boldsymbol{\theta}(k)} q^*(k)\Big\} \tag{19}$$

leading to a simple stochastic approximation of the form:

$$\hat{\mathbf{h}}(k) = \lambda_{ch}\hat{\mathbf{h}}(k-1) + (1-\lambda_{ch})\mathbf{v}(k) \cdot e^{-j\boldsymbol{\theta}(k)} q^*(k) \tag{20}$$

where λ_{ch} is an exponential forgetting factor. For the i.i.d. Gold code sequences, optimal tap selection through truncation in magnitude is readily achieved [14].

b) Recursive interference-free signal reconstruction: Under inter-chip-interference (ICI)—be it caused by the time-varying Doppler distortion w.r.t chips within an entire code, or due to multipath—equation (15) can be expanded as

$$\mathbf{v}(k) = \left[\mathbf{h}[0]q[k] + \sum_{m\neq 0} \mathbf{h}[m]q[k-m]\right] \cdot e^{j\boldsymbol{\theta}(k)} + \mathbf{w}(k) \tag{21}$$

The ICI signal is defined as

$$\mathbf{v}_{ICI}(k) \triangleq \sum_{m\neq 0} \mathbf{h}[m]q[k-m] \cdot e^{j\boldsymbol{\theta}(k)} \tag{22}$$

and the ICI-free signal as

$$\mathbf{v}_0(k) \triangleq \mathbf{h}[0]q[k] \cdot e^{j\boldsymbol{\theta}(k)} + \mathbf{w}(k) \tag{23}$$

The composite signal, not counting the noise, can thus be expressed as

$$\begin{aligned} \bar{\mathbf{v}}(k) &\triangleq \sum_{m=0}^{L-1} \mathbf{h}[m]q[k-m] \cdot e^{j\boldsymbol{\theta}(k)} \\ &= \mathbf{v}_{ICI}(k) + \mathbf{h}[0]q[k] \cdot e^{j\boldsymbol{\theta}(k)} \end{aligned} \tag{24}$$

Adding and subtracting a $\mathbf{h}[0]q[k] \cdot e^{j\boldsymbol{\theta}(k)}$ term from the RHS of equation (21) gives:

$$\begin{aligned} \mathbf{v}(k) &= \mathbf{v}_0(k) + \mathbf{v}_{ICI}(k) \\ &= \mathbf{v}_0(k) + \bar{\mathbf{v}}(k) - \mathbf{h}(k)q[k] \cdot e^{j\boldsymbol{\theta}(k)} \end{aligned} \tag{25}$$

In addition, $\bar{\mathbf{v}}(k)$ obeys a shifting law such that

$$\bar{\mathbf{v}}(k) = \begin{bmatrix} \bar{\mathbf{v}}_{L-1}(k) \\ \downarrow^{N_s} \quad \bar{\mathbf{v}}(k-1) \end{bmatrix} \tag{26}$$

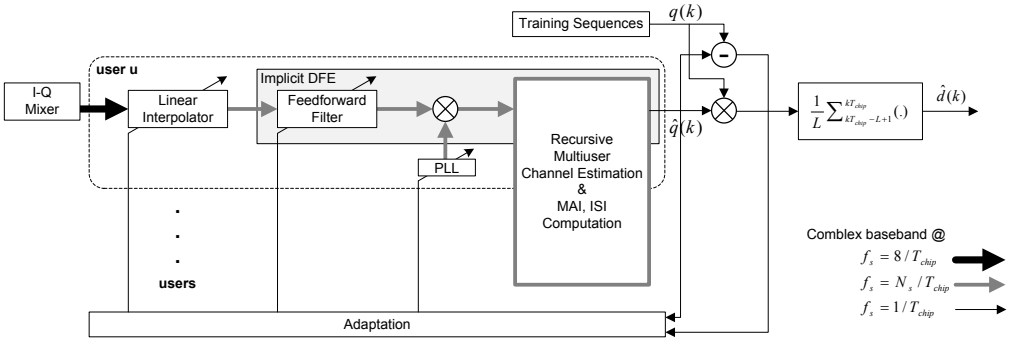

Fig. 6: The overall tracker for ABU.

where

$$\underline{\bar{\mathbf{v}}}_{L-1}(k) = \sum_{m=0}^{L-1} q[k+m]\underline{\mathbf{h}}_m(k) \tag{27}$$

and $\downarrow^{N_s} \bar{\mathbf{v}}(k-1)$ symbolizes down-shifting by N_s samples.

Replacing the channel vector by its estimate, we arrive at a channel adaptation procedure that can be performed in two coupled steps. Firstly, equation (25) is rearranged so as to allow the *reconstruction* of an estimate of the ICI-free signal:

$$\hat{\mathbf{v}}_0(k) = \mathbf{v}(k) - \hat{\bar{\mathbf{v}}}(k) + \hat{\mathbf{h}}(k)q[k] \cdot e^{j\hat{\boldsymbol{\theta}}(k)} \tag{28}$$

Secondly, using the ICI-free signal in (20) for better channel estimation yields

$$\hat{\mathbf{h}}(k) = \lambda_{ch}\hat{\mathbf{h}}(k-1) + (1-\lambda_{ch})\hat{\mathbf{v}}_0(k)q^*[k] \tag{29}$$

Once the channel estimate and the ICI-free signal have been computed, the chip estimate is defined by the filtering operation

$$\hat{q}(k) = \frac{1}{E_{\hat{\mathbf{h}}}(k)}\hat{\mathbf{h}}'(k)\hat{\mathbf{v}}_0(k) \tag{30}$$

where

$$E_{\hat{\mathbf{h}}}(k) = \hat{\mathbf{h}}'(k)\hat{\mathbf{h}}(k) \tag{31}$$

This model allows us to monitor the state of self-interference explicitly. It can be shown [13] that this formulation can be expanded in the multiuser case to account for multiple access interference (MAI), albeit at the expense of increased computation complexity and memory requirements. Specifically, with a total of U users present in the system, the recursive reconstruction of the average signal vector becomes

$$\underline{\bar{\mathbf{v}}}_{L-1}(k) = \sum_{u=1}^{U} \underline{\bar{\mathbf{v}}}^u_{L-1}(k) \tag{32}$$

where

$$\underline{\bar{\mathbf{v}}}^u_{L-1}(k) = \sum_{m=0}^{L-1} q^u[k+m]\underline{\mathbf{h}}^u_m(k) \tag{33}$$

with the superscript ^{u} denoting the u^{th} user's reconstructed signal, spreading code, and channel vector.

c) Acquisition test: Monitoring the MSE of a running despreader provides a measure of signal-to-noise-plus-interference ratio (SNIR) at the output:

$$\hat{d}(k) = \mathbf{E}\{\hat{q}(k)q^*(k)\} = \frac{1}{L}\sum_{m=k-L+1}^{k} \hat{q}(m)q^*(m) \tag{34}$$

$$e_{\hat{d}}(k) = 1 - \hat{d}(k), SNIR_{out} \sim \mathbf{E}\{|e_{\hat{d}}(k)|^2\} \tag{35}$$

$$SNIR_{out}(k) = -10\log_{10}\left(\frac{1}{N_d}\sum_{m=k-N_d+1}^{k}|e_{\hat{d}}(m)|^2\right) \tag{36}$$

where N_d is the length of despreader observation.

Once the MSE drops below a pre-specified threshold, it can be used as an indication for successful acquisition.

2) Implicit DFE Extension: Applying a decision feedback equalizer (DFE) to $\mathbf{v}(k)$ at the chip-rate, as if no spreading is taking place, a chip estimate can be expressed as

$$\hat{q}(k) = \mathbf{a}'\mathbf{v}(k) - \mathbf{b}'\mathbf{q}(k-1) \tag{37}$$

where $\mathbf{a}$ and $\mathbf{b}$ are the feedforward and feedback coefficient vectors respectively, and $\mathbf{q}(k-1)$ is the vector of the previously searched chips (during acquisition) whose length is in accordance with distortion span in chips M.

$$\mathbf{q}(k-1) = \begin{bmatrix} q[k-1] & \cdots & q[k-M] \end{bmatrix}^T \tag{38}$$

If we substitute our signal model (15) into (37) and neglect the noise for the moment, we obtain

$$\hat{q}(k) = \left[\mathbf{a}'\hat{\mathbf{h}}[0]q[k] + \mathbf{a}'\sum_{m>0}\hat{\mathbf{h}}[m]q[k-m]\right] \cdot e^{j\hat{\boldsymbol{\theta}}(k)} - \mathbf{b}'\mathbf{q}(k-1) \tag{39}$$

Inspecting equation (39) implies that

$$\mathbf{b}' = \mathbf{a}'\sum_{m>0}\hat{\mathbf{h}}[m] \cdot e^{j\hat{\boldsymbol{\theta}}(k)} \tag{40}$$

is required so that the ICI contribution to the chip estimate be eliminated. In other words, the task of backward filtering is readily taking place through shifts of the channel estimate,

where we assumed that the channel is zero outside the *multipath span*, i.e.

$$\hat{h}_n(k) = 0, \quad n > M \tag{41}$$

Equally, we can substitute (25) into (37) to obtain

$$\hat{q}(k) = \mathbf{a}'\hat{\mathbf{v}}_{0}(k) + \mathbf{a}'\hat{\mathbf{v}}_{ICI}(k) - \mathbf{b}'\mathbf{q}(k-1) \tag{42}$$

$$= \mathbf{a}'\hat{\mathbf{v}}_{0}(k) + \mathbf{a}'\hat{\tilde{\mathbf{v}}}(k) - \mathbf{a}'\hat{\mathbf{h}}(k)q[k]\cdot e^{j\boldsymbol{\theta}(k)} - \mathbf{b}'\mathbf{q}(k-1) \tag{43}$$

Comparing equations (43), (39), and (28), one notices that it is possible to further filter the incoming signal $\mathbf{v}(k)$ with a linear adaptive equalizer $\mathbf{a}'(k)$ *independent of* $\hat{\mathbf{h}}(k)$ in order to obtain an improved chip estimate at time kT_c. The clean chip estimate is defined by the term containing the reconstructed ICI-free feedforward signal—which is *dependent upon* the goodness of the channel estimate

$$\hat{q}(k) = \mathbf{a}'(k)\hat{\mathbf{v}}_{0}(k) \tag{44}$$

The combined operation effectively realizes an *implicit* DFE wherein the separation of the incoming signal into forward and backward components is denoted by the subscripts $_f$ and $_b$ respectively.

Equating (44) and (30) is interesting:

$$\mathbf{a}'(k) = \frac{1}{E_{\hat{\mathbf{h}}}(k)}\hat{\mathbf{h}}'(k) \tag{45}$$

In the absence of *multipath*, the sole role of $\mathbf{a}'(k)$ would be to combat *phase* distortion in the fractional chip fed into the spread spectrum algorithm. Equation (45) tells us that if the channel alone fails at equalizing the chip estimate perfectly, the feedforward filter of the implicit DFE would help in accomplishing the task by eliminating residual distortion. This is especially the case for a highly-Doppler-susceptible, non-stationary indoor acoustic environment.

To this end and with the intuition of equation (45) in mind, the *modified* fractional feedforward filter (FF) is made to operate on incoming chips at the oversampling rate with N_s samples per chip, although its adaptation remains at the chip rate such that

$$v(t) = \sum_{m}^{L_{ff}} a(mT_c/N_s)s(t - mT_c/N_s) \tag{46}$$

where $s(t)$ is instead the raw complex baseband signal at the receiver now. In vector format, we define

$$\underline{\mathbf{c}}(k) \triangleq \left[c_{N_s}(k) \ \cdots \ c_1(k)\right]^T \tag{47}$$

to be an oversampled chip of N_s entries at time kT_c , and

$$\underline{\mathbf{v}}(k) \triangleq \left[\mathbf{a}'(k)\begin{bmatrix} c_{N_s}(k) & \cdots & c_1(k) \\ \vdots & \iddots & \downarrow^1 \mathbf{s}(k-1) \\ c_1(k) & \iddots & \\ \downarrow^{N_s}\mathbf{s}(k-1) & & \end{bmatrix}\right]^T \tag{48}$$

to be the modified fractional feedforward filtering at time kT_c. The length of the filter is designed to span a certain number of oversampled chips L_{ff}, and is devoted to combating phase distortion by means of matching the filter response to the incoming signal. Inevitably, it also introduces ICI which will be leaked away by the sparse channel-based backward filtering and futher combated within the interference cancellation in equation (43).

The LMS-adapted FF filter is given by

$$\hat{\mathbf{a}}(k+1) = \hat{\mathbf{a}}(k) + \mu_{LMS}\ e^*_{\hat{q}}(k)\ e^{-j\hat{\theta}(k)}\ \mathbf{s}(k) \tag{49}$$

3) Integrated Second-order PLL: The signal baseband model (15) includes an explicit term to account for transmitter-receiver phase variations at the chip rate. While these variations are due to mismatch and/or node mobility, they also affect the order-comparable carrier and code frequencies. This phase term is estimated using a second-order, stochastic gradient phase-locked loop (PLL) according to the MMSE criterion of the chip estimate as follows.

The chip estimate error is first generated

$$e(k) = q[k] - \hat{q}(k) \tag{50}$$

The gradient is then shown to be [16]

$$\frac{\partial|e^2(k)|}{\partial\hat{\theta}} = 2\ \mathrm{Re}\left\{\frac{\partial e(k)}{\partial\hat{\theta}}e^*(k)\right\}$$

$$= -2\ \mathrm{Im}\left\{\frac{1}{E_{\hat{\mathbf{h}}}(k)}\hat{\mathbf{h}}'(k)\left[\dot{\mathbf{v}}(k)\cdot e^{-j\hat{\boldsymbol{\theta}}(k)}\right]e^*(k)\right\} \tag{51}$$

where $\dot{\mathbf{v}}(k)$ is the chip-by-chip, adaptively forwarded vector. The PLL is then implemented as

$$\psi(k) = \mathrm{Im}\left\{\frac{1}{E_{\hat{\mathbf{h}}}(k)}\hat{\mathbf{h}}'(k)\left[\dot{\mathbf{v}}(k)\cdot e^{-j\hat{\boldsymbol{\theta}}(k)}\right]e^*(k)\right\}$$

$$\hat{\theta}(k+1) = \hat{\theta}(k) + K_1\psi(k) + K_2\sum_{m\le k}\psi(k) \tag{52}$$

where K_1 and K_2 are the loop constants and often chosen such that $K_2 = K_1/10$.

4) Linear Interpolation Stage: Under the narrowband assumption, the Doppler effect can be sufficiently modelled as a frequency shift. On the contrary, in wideband signals the ideal model is better represented by an accurate rate change operation [15]

$$r(nT_s) = s\big((1+\delta)nT_s\big) \tag{53}$$

The removal of the non-uniform Doppler shift across the spectral content of the wideband signal is then performed as a sampling frequency rescaling operator

$$f_s = (1+\delta)f_s^D \tag{54}$$

where f_s^D is the original sampling frequency of the receiver at which the Doppler effect is manifest.

The framework afforded by the DS CDMA adaptive engine derived earlier facilitates a front-end linear interplator (LI)

stage, also operating at the chip rate, that can seamlessly plug into the global cooperative MSE minimization criterion.

To this end, we define a *time-varying* stage that linearly interpolates the incoming complex baseband signal in accordance with a cost function driven by the core DS CDMA demodulator. In order to minimize the distortion introduced by linear interpolation, the complex baseband signal is well oversampled and decimation occurs tacitly, i.e. all oversamples participate in interpolation.

In a decision-directed mode, the maximum likelihood (ML) carrier phase estimator for the signal $s(t;\phi)$ with a known information sequence $\{I_n\}$ is given by [11, p. 304]

$$\hat{\phi}_{ML} = -\tan^{-1}\left[\mathrm{Im}\left(\sum_{n=0}^{K-1} I_n^* y_n\right) \Big/ \mathrm{Re}\left(\sum_{n=0}^{K-1} I_n^* y_n\right)\right] \tag{55}$$

where y_n is the output of the matched filter in the n^{th} signal interval T, and K is a positive integer defining the observation interval $T_0 = KT$. Therefore, in a similar fashion [17], the interpolation factor is adapted per step as

$$I(k+1) = I(k) + K_p\, \phi(k) \tag{56}$$

where K_p is a phase tracking constant, and $\phi(k)$ is the ML phase estimate. Within our code acquisition DS CDMA formulation, $\phi(k)$ is updated at the chip rate using the chip phase as opposed to the symbol phase

$$\phi(k) = \angle \hat{q}(k) \tag{57}$$

C. Motion inference

1) First-order moment—Velocity: Velocity inference is accomplished through the estimation of the the instantaneous frequency. The procedure for estimating IF varies depending on the tracking configuration.

a) DFE-PLL: In the joint DFE-PLL mode, there is an apparent phase tracking redundancy. In underwater acoustic (UWA) systems, PLL's tracking constants are made substantially higher than the FF's learning rate—which is characterized by its length and percentage of error feedback—such that the PLL dominates the FF equalizer [18]. In the ABU band, a special case arises when a competition between the feedforward complex filter and the second-order PLL is allowed. When both attempt to compensate for Doppler-induced phase distortion in near-equal strengths, it was observed empirically that the unwrapped phase of the chip estimates is no longer a monotonically increasing function. Rather, the unwrapped phase possesses some notable attributes that are correlated with motion:

1) It tends to inflect upon reversal of acceleration.
2) It drifts during motion pauses with a certain slope.
3) Provided that the responsiveness of the DFE-PLL configuration is tuned accordingly, the range covered by the unwrapped phase, in a time interval of continuous motion, is very close to the limit of the speed in that motion segment. This can be ascertained by converting the unwrapped phase into a unitless turns-per-second entity according to the direct weighing

$$\Omega_i(k) = \frac{c}{f_{carr}}\,\frac{1}{2\pi}\,\phi_{chip}(k) \tag{58}$$

where Ω_i is the weighted instantaneous phase, measuring the turns per second that the phase makes throughout the course of the periodic motion stimulus.
4) The shape of the unwrapped phase is also a function of the responsiveness of this competition.

These observations seem to suggest that the unusual competition between the PLL and DFE in tracking the phase results readily in a *measure* of the instantaneous frequency.

However, the low ABU speed of propagation is even less than one fourth that of the underwater environment. The time-dilation or compression that airborne acoustics undergo is of the same order (up to a tenth of the center frequency) often encountered in RF inter-satellite communications. This is best visualized by examining the Doppler shift formula $f_{dv} \uparrow = f\ \frac{v\uparrow}{c\downarrow}$ that translates increased velocity into accentuated Doppler shift. Moreover, the order-comparable chip rate further exasperate the Doppler distortion.

Thus the ultra high velocities in the ABU band would strain even a combined DFE-PLL equalizer being updated at the chip rate. Among the symptoms of such strain are excessive equalizer tap rotation and possible phase tracking loop instability [19]. This strain calls for *leaky* adaptive techniques [20] for FF as to aid stability, tracking, and combat drift.

Building on adaptive filtering concepts [21, p. 384-387] and techniques [22], we introduce the following *ad hoc* perturbation to the standard LMS adaptation criterion. We dub this arrangement Doubly Reinforced Code Epoch (DRCE) and define it as follows: Once every code period, the last chip is skipped and replaced by the first incoming chip which is consequently used to generate the adaptation error. The next iteration proceeds normally at the first chip again. This effectively injects data-dependent perturbation to weights. The modification introduced to the circular Gold sequence at time kT_c is simply

$$\mathbf{q}(k) = \big[q[k]\ \cdots\ q[k-L+2]\ q[k-L]\big]^T \tag{59}$$

where $q[k] = q[k-L]$.

From empirical grounding, it was found that this *ad hoc* technique has a critical effect on Doppler tracking for the DFE-PLL configurations.

A less formal inspiration for DRCE leaky adaptation can be found in the domain of pedestrian tracking using inertial sensors. According to the so-called zero-velocity updates (ZUPT) criterion, at the end of each estimation cycle, the velocity is set to zero upon detection of a stance phase in order to prevent excessive error growth in the navigation model [23]. This is vaguely related to DRCE—observing the periodicity of back-to-back code transmissions, DRCE injects a cyclic perturbation to weights on a code-by-code basis. However, in DRCE, the perturbation is derived from the incoming data too.

b) DFE-LI: Despite LI's agility in tracking Doppler, distortion introduced by linear interpolation needs to be dealt with. The matched filtering properties of the FF readily provides an equalizing effect for a variety of distortion sources. Therefore, the LI-DFE combination represents a very viable phase tracking mechanism whereby:

1) The interpolation factor's polarity determines the direction of movement: backward or and forward.

$$I_{sgn}(k) = \mathrm{sgn}\big(I(k)\big) \tag{60}$$

I_{sgn} is then used to delimit the motion segment and velocity estimation is performed as

$$v_i(k) = \frac{c}{f_{carr}} \frac{1}{2\pi} \frac{\phi^u_{chip} - \phi^l_{chip}}{t^u - t^l} \tag{61}$$

where the superscripts ^{u} and ^{l} denote respectively the upper and lower bounds of the motion segment as determined by I_{sgn}.

2) Minimal tap translation and rotation per motion segment takes place in FF since LI will dominate phase tracking.
3) Acceleration and/or jerk can tip the balance of LI such that the interpolation factor will not return to rest. In this case, the FF will intervene briefly to adjust the phase resulting in ambiguity in the measured rate of change from the slope of the unwrapped phase of the chip estimate.

2) Second-order moment—Acceleration stress: The adaptive estimation of instantaneous acceleration (IA) is desirable. This desirability is because online mechanisms for the inference of additional physical properties of motion (e.g. acceleration) could add to the richness of the sensory model and allow for sophisticated workarounds in the presence of higher motion moments in the ABU band.

The IA estimator for coherent ABU is developed here in analogy with a single-tone, frequency-modulated (FM) signal. Specifically, we note that the running despreader $\hat{d}(k)$ in equation (34) can be thought of as a *phasor* at any given time kT_c. This phasor represents a measure of how much, after demodulation, the receiver code is in-lock with the undistorted transmitted code. The rate of change in the demodulated despreader phase is now associated with the second motion moment, acceleration. That is, the complex depreader is already a first-order statistical moment of the chip estimates, which in turn can be seen as a complex-valued random variable (note the expectation operator in equation (34)). The despreader phasor can therefore be modelled in the continuous-time domain as

$$z_{\hat{d}}(t) = a_{\hat{d}}(t)\, e^{j\phi_{\hat{d}}(t)} = x_{\hat{d}}(t) + j\, y_{\hat{d}}(t) \tag{62}$$

with

$$\phi_{\hat{d}}(t) = 2\pi \int_{-\infty}^{t} f'_i(\tau)\, d\tau \tag{63}$$

and $f'_i(t)$ denoting the time-varying, second-order instantaneous frequency.

Differentiating the despreader phase, using the classic continuous-time formula for FM discriminators [24], yields the discrete-time estimator

$$\hat{f}'_i(k) = \frac{1}{2\pi} \frac{x_{\hat{d}}(k) y'_{\hat{d}}(k) - x'_{\hat{d}}(k) y_{\hat{d}}(k)}{x^2_{\hat{d}}(k) + y^2_{\hat{d}}(k)} \tag{64}$$

For a convergent $\hat{d}(k)$ i.e. after acquisition has been declared and tracking has begun, a number of approximations hold. First, if $\mathrm{Re}\{\hat{d}(k)\}$ is stable, then $x_{\hat{d}}(k) \approx 1$, $x'_{\hat{d}}(k) \approx 0$, and $x^2_{\hat{d}}(k) \approx 1$. Second, if phase lock is maintained, $y^2_{\hat{d}} \approx 0$. These approximations lead to the following second-order IF estimator in our ABU system

$$\hat{f}'_i(k) \propto \frac{1}{2\pi}\, y'_{\hat{d}}(k) \tag{65}$$

The second-order IF component is proportional to the rate of change (first derivative) of the imaginary part of the running despreader. In expression (65), equality is substituted for proportionality bearing in mind the limited code-length average which is provided by the running despreader. That is, additional processing (such as exponential statistical weighting) will be required if we were to convert this unitless entity into a meter-per-second-squared instantaneous acceleration estimator.

The final IA estimator is then obtained by scaling the second-order IF component according to

$$a_i(k) = \frac{c}{f_{carr}}\, \hat{f}'_i(k) \tag{66}$$

IV. Experimental Results

A. Signal Design and Experimental Setup

A Gold code of length 511 was BPSK-modulated onto a 50 kHz carrier at a 20 kHz chip rate. Chips were pulse-shaped using a raised-cosine filter with roll-off factor of 1. The sampling rate utilized was 160 kHz.

One data set will be used for the characterization of the two algorithmic configurations. This data set has typical maximum speed (about 0.8 m/sec) and contains high-order motion moments. In order to facilitate characterization, we utilize a vision-based tracking system for the generation of real-time position and speed ground truth. A transmitter is mounted on a Lego Mindstorms robot moving forward and backward on a track while facing a stationary ABU receiver, at a distance of 2.9 m. The robot is tagged with a fiducial marker [25]. A PC-based application monitors the movement of the robot using the computer vision-based tracking. Upon motion, the application triggers an FPGA-based ABU transmitter and simultaneously commences data acquisition. The all-digital transmitter has an independent oscillator to the PC clock. The experimental setup used for data collection is shown in figure 8.

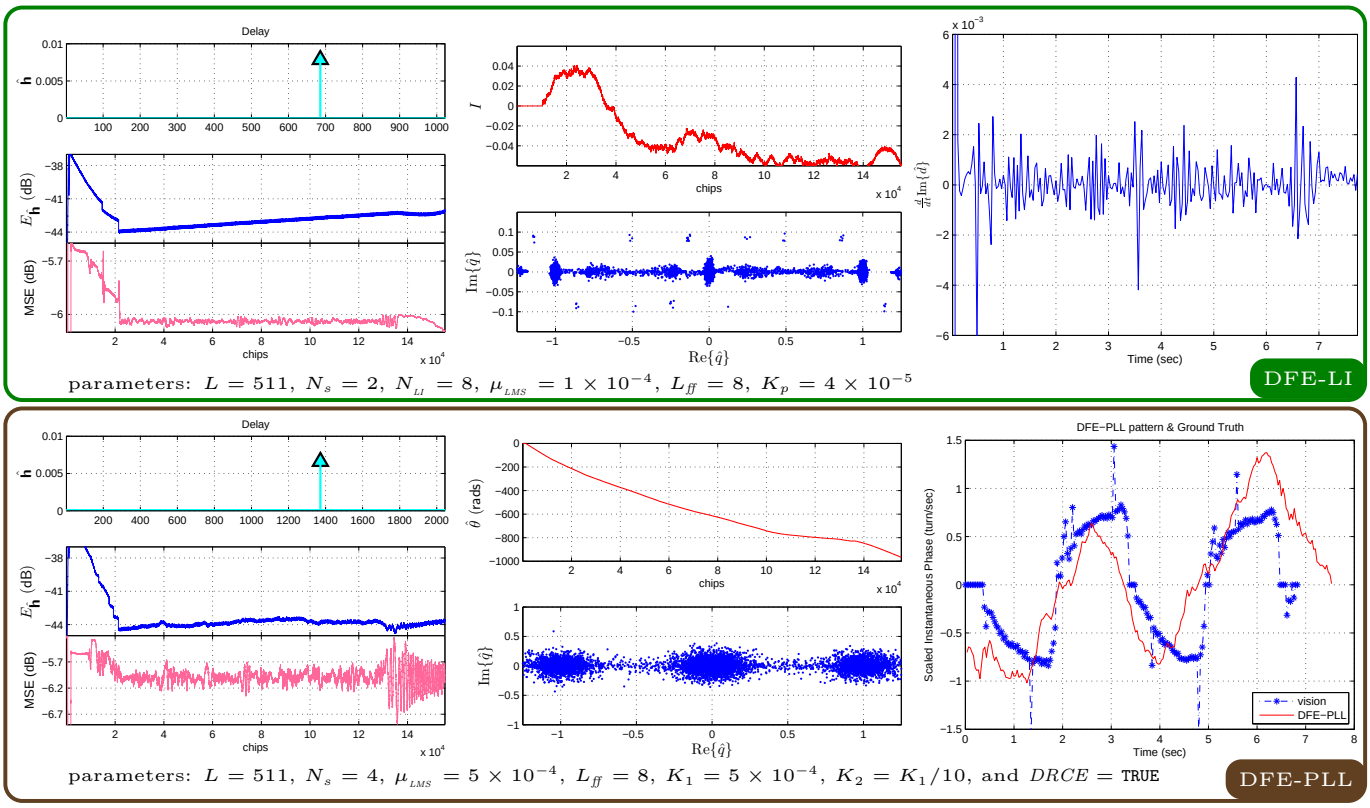

Fig. 7: Tracking performances: upper row DFE-LI and lower row DFE-PLL.

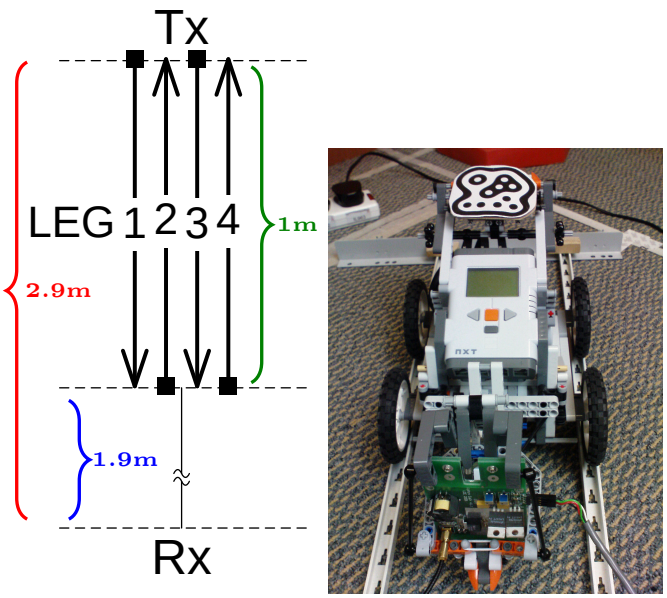

(a)

(b)

Fig. 8: Experimental setup. (a) Transmitter path moving forward and backward while facing a stationary receiver. (b) Lego Mindstroms robot with mounted transmitter.

B. *Performance*

The acquired signal was down-converted to baseband where all processing takes place. Figure 7 illustrates the performance of the DFE-LI and DFE-PLL tracking configurations. The upper set of plots belong to DFE-LI. The first plot shows the channel which is maintained throughout tracking. The adaptation mean-square error (MSE) begins its decent initially until tacking reaches a steady-state around 1 sec. The second plot depicts of the evolution of the linear interpolation factor in time and the chip estimate scatter. The sensitivity of the DFE-LI tracker to acceleration and jerk was avoided initially by a priori knowledge of the Doppler stimulus. As such, the instance at which LI is activated was delayed. As shown, DFE-LI tracks Doppler very accurately during the first and most of the second motion legs. The velocity for the first motion segment was estimated to be 0.8047 m/s, which is virtually identical to ground truth. However, following the decelerating motion moments in the second leg, LI diverges away from rest condition owing to high second-order motion stresses. The third plot examines this stress resulting from second-order motion moments. The IA estimator shows distinct sustained acceleration spikes in three places: at the beginning of the Doppler stimulus around 0.5 sec; around the momentary pause of the robot at roughly 3.5 sec between leg 2 & leg 3; and at the end of the test case slightly before 7 sec. These instances are in line with the acceleration groundtruth of the Doppler stimulus.

Similarly, the performance of the DFE-PLL tracking configuration is illustrated in the second row of plots of figure 7.

Justifiably, the crude DFE-PLL tracker is noisier even though code timing stays in-lock. In the second plot the PLL phase evolution is shown alongside the chip estimate scatter, which is considerably more spread in comparison to that of the DFE-LI configuration. The third plot shows the scaled unwrapped phase of the chip estimate overlaid on the vision tracking ground truth. The scaled instantaneous phase is evidently correlated with motion in this competitive mode, which provides a crude means for estimating velocity. This method for inferring the motion pattern could be useful in certain applications not requiring precise velocity measurements.

V. Conclusion

This paper has given a novel characterisation of the ABU channel, providing a summary of expectations for signal-to-noise ratio, channel bandwidth and capacity, for typical indoor office conditions. Real-world ABU location systems require Doppler tracking in order to cope with typical indoor movements. This paper has developed the first Doppler-tolerant ABU tracker (figure 6). It is based around an implicit decision feedback equaliser, incorporating a feedforward filter which has been modified to operate on incoming chips at the oversampling rate. The DFE works in conjunction with two other blocks: (1) an integrated second-order PLL to estimate phase variations (due to mismatch or node mobility); and (2) a linear interpolator which models Doppler shift as a rate change operation. Methods for computing the first– and second-order moments (velocity and acceleration) were also presented.

The ABU Doppler tracker is thus an *hybrid* one, operating as DFE-PLL or DFE-LI. Experimental analysis shows that the DFE-PLL tracker stays locked on, but produces noisier chip estimates and can only give a crude indication of velocity based on its unwrapped, scaled instantaneous phase. By contrast, the DFE-LI variant can produce highly accurate velocity estimates, but tends to lose track in the presence of significant acceleration and jerk.

References

[1] See for instance commercial systems from *InterSense Inc.*, *Ascension Technology Corp.*, and *Ubisense Ltd.*

[2] M. McCarthy, P. Duff, H. L. Muller, and C. Randell, "Accessible Ultrasonic Positioning," *IEEE Pervasive Computing*, vol. 5, no. 4, pp. 86–93, 2006.

[3] M. Hazas and A. Hopper, "Broadband ultrasonic location systems for improved indoor positioning," *IEEE Transactions on Mobile Computing*, vol. 5, no. 5, pp. 536–547, May 2006.

[4] M. Toda and S. Tosima, "Theory of curved, clamped, piezoelectric film, air-borne transducers," *IEEE Transactions on Ultrasonics, Ferroelectrics, and Frequency Control*, vol. 47, no. 6, pp. 1421–1431, nov 2000.

[5] J. Gonzalez and C. Bleakley, "High-Precision Robust Broadband Ultrasonic Location and Orientation Estimation," *Selected Topics in Signal Processing, IEEE Journal of*, vol. 3, no. 5, pp. 832–844, Oct. 2009.

[6] F. J. Álvarez, J. Ureña, M. Mazo, A. Hernández, J. J. García, and C. de Marziani, "High reliability outdoor sonar prototype based on efficient signal coding," *IEEE Transactions on Ultrasonics, Ferroelectrics, and Frequency Control*, vol. 53, no. 10, pp. 1862 –1872, Oct. 2006.

[7] C. Li, D. Hutchins, and R. Green, "Short-range ultrasonic communications in air using quadrature modulation," *IEEE Transactions on Ultrasonics, Ferroelectrics, and Frequency Control*, vol. 56, no. 10, pp. 2060–2072, October 2009.

[8] M. Stojanovic, "On the relationship between capacity and distance in an underwater acoustic communication channel," *SIGMOBILE Mob. Comput. Commun. Rev.*, vol. 11, pp. 34–43, October 2007.

[9] International Organization for Standardization, *Acoustics—Attenuation of sound during propagation outdoors—Part 1: Calculation of the absorption of sound by the atmosphere*. Geneva, Switzerland: ISO 9613-1, 1993.

[10] American National Standards Institute, Committee S1, *Acoustics—Method for Calculation of the Absorption of Sound by the Atmosphere*, ser. ANSI S1.26-1995. 1430 Broadway, New York, NY 10018, USA: American National Standards Institute, September 1995.

[11] J. Proakis and M. Salehi, *Digital Communications*, 5th ed. McGraw-Hill, November 6 2007.

[12] M. Alloulah, "Real-Time Tracking for Airborne Broadband Ultrasound," PhD Dissertation, School of Computing and Communications, Lancaster University, LA1 4WA, June 2011.

[13] M. Stojanovic and L. Freitag, "Multiuser code acquisition in multipath channels," in *Oceans 2005 - Europe*, vol. 1, June 2005, pp. 74–79.

[14] M. Stojanovic, "Efficient processing of acoustic signals for high-rate information transmission over sparse underwater channels," *Physical Communication*, vol. 1, no. 2, pp. 146 – 161, 2008.

[15] B. Sharif, J. Neasham, O. Hinton, and A. Adams, "A computationally efficient doppler compensation system for underwater acoustic communications," *IEEE Journal of Oceanic Engineering*, vol. 25, no. 1, pp. 52–61, jan 2000.

[16] M. Stojanovic, J. Catipovic, and J. Proakis, "Phase-coherent digital communications for underwater acoustic channels," *IEEE Journal of Oceanic Engineering*, vol. 19, no. 1, pp. 100–111, Jan 1994.

[17] B. Sharif, J. Neasham, O. Hinton, A. Adams, and J. Davies, "Adaptive doppler compensation for coherent acoustic communication," *Radar, Sonar and Navigation, IEE Proceedings* -, vol. 147, no. 5, pp. 239 –246, Oct. 2000.

[18] M. Johnson, L. Freitag, and M. Stojanovic, "Improved doppler tracking and correction for underwater acoustic communications," in *Acoustics, Speech, and Signal Processing, (ICASSP), IEEE Int'l Conf. on*, vol. 1, Apr. 1997, pp. 575–578.

[19] B. Sharif, J. Neasham, O. Hinton, and A. Adams, "Closed loop doppler tracking and compensation for non-stationary underwater platforms," in *OCEANS 2000 MTS/IEEE Conference and Exhibition*, vol. 1, Sept 2000, pp. 371–375.

[20] R. Gitlin, H. Meadors, and S. Weinstein, "An algorithm for the stable operation of a digitally-implemented fractionally-spaced adaptive equalizer," in *Acoustics, Speech, and Signal Processing, IEEE Int'l Conf. on ICASSP '82.*, vol. 7, May 1982, pp. 1379–1383.

[21] A. H. Sayed, *Adaptive Filters*, hardcover ed. Wiley-IEEE Press, May 2008.

[22] V. Nascimento and A. Sayed, "Unbiased and stable leakage-based adaptive filters," *Signal Processing, IEEE Transactions on*, vol. 47, no. 12, pp. 3261–3276, Dec 1999.

[23] E. Foxlin, "Pedestrian tracking with shoe-mounted inertial sensors," *Computer Graphics and Applications, IEEE*, vol. 25, no. 6, pp. 38–46, nov.-dec. 2005.

[24] F. J. Harris, "Exact FM detection of complex time series," in *ISSPA '87*, Brisbane, Australia, 1987, pp. 70–73.

[25] reacTIVision 1.4, , accessed 10 April 2011.